

Highlights

A Novel Numerical Model for Detailed Simulation of CO₂ Capture

Sajad Jafari, Ran Yao, Salar Zamani Salimi, Luca Brandt, Christophe Duwig

- We present a novel coupling method for simulation of interfacial mass transfers in vapor-liquid systems with chemical reactions within the phase field framework.
- We show detailed simulations of CO₂ capture by an aqueous solvent with non-ideal thermophysical properties at phase equilibrium and chemical reactions, giving new insights at the droplet scale.
- The equilibrium condition is implemented for capturing with precision the interface conditions, i.e. heat- and mass-transfer from both liquid-to-vapor and vapor-to-liquid processes, thus ensuring a consistent overall species concentration.
- The method is demonstrated with a non-ideal solvent solution (MDEA) for CO₂ capture and features CO₂ capture by multiple droplets with varying MDEA concentration.

A Novel Numerical Model for Detailed Simulation of CO₂ Capture

Sajad Jafari^{a,*}, Ran Yao^a, Salar Zamani Salimi^b, Luca Brandt^{b,c}, Christophe Duwig^a

^a*Department of Chemical Engineering Royal Institute of Technology (KTH) Stockholm Sweden*

^b*Department of Energy and Process Engineering Norwegian University of Science and Technology (NTNU) Trondheim Norway*

^c*Department of Environment Land and Infrastructure Engineering (DIATI) Politecnico di Torino Torino Italy*

Abstract

According to the Intergovernmental Panel on Climate Change, CO₂ capture using liquid absorbents is a key strategy for mitigating climate change. However, the energy footprint of the technique is still high and novel solutions are needed to design better units. To that end, this study presents a novel and detailed diffuse-interface model for interfacial mass and heat transfer coupled with chemical reactions for CO₂ capture. Two scalar transport equations describe the species evolution in each phase, coupled through a variable apparent Henry's constant that captures non-ideal vapor–liquid equilibrium at the interface. Momentum and energy transport are modeled through single-scalar formulations, with interfacial velocity discontinuities arising from reactive phase change, handled via a Stefan condition. A conservative phase-field method closes the equations, with regularization applied to suppress numerical diffusion when tracking the interface. The model resolves key physical phenomena, including reaction kinetics, mass transfer resistance, H₂O phase change, and interfacial velocity jumps during both absorption and desorption. A sensitivity analysis shows that increasing the solvent mole fraction enhances chemical reactivity but increases diffusive resistance, inducing complex nonlinear effects on the interfacial reactive transport. The coupled CO₂ and H₂O interphase transport are captured simultaneously, with water evaporation shown to have limited impact on CO₂ uptake and on the interfacial reactive Stefan velocity for isolated droplets. Additionally, multi-droplet simulations demonstrate that the droplet number and an imposed gas-phase mean flow significantly affect absorption rates and spatial asymmetry through droplet-droplet interactions and convective transport. The findings offer critical insights into interfacial CO₂ transport in reactive, two-phase systems and supports the need for advanced numerical studies like the present one, given the lack of droplet-scale data and the limited applicability of bulk-scale experiments to localized transient interfacial processes.

Keywords: CO₂ capture, Reactive mass transfer, Phase change, Stefan flow, Diffuse-interface

*Corresponding author: sajadja@kth.se

1. Introduction

The urgent need to mitigate climate change has driven the development of Carbon Capture and Storage (CCS) technologies, which are essential for achieving the UN Sustainable Development Goals, particularly SDG7 (Affordable and Clean Energy) and SDG13 (Climate Action), through the reduction of industrial carbon emissions [1, 2]. Among the various CO₂ capture technologies, spray towers stand out as a future solution because of their high mass transfer efficiency and scalability, although packed columns remain the benchmark technology [3, 4].

1.1. Previous Studies- Research Gap

CO₂ capture in spray towers has primarily attracted experimental investigations, focusing on optimizing factors such as solvent kinetics, nozzle design, spray patterns, and liquid-to-gas ratios [5–7]. These studies have mainly aimed at enhancing the device performance by manipulating nozzle geometry and spray characteristics to optimize droplet size distribution, which plays a key role in mass transfer and CO₂ capture efficiency [8, 9]. However, these works often lack a comprehensive understanding of the column dynamics and the underlying physics of the CO₂ capture process, particularly the complex interactions between mass transfer, chemical reactions, and the behavior of reactive multiphase systems. This gap underscores the need for novel numerical models that can capture these interactions in greater detail, as they are challenging to investigate experimentally. Today, many researchers and engineers continue to adopt simplified methodologies, such as Euler-Lagrange frameworks and empirical correlations [10–12]. These approaches establish an approximate relationship between the gas-phase mass transfer coefficient (k_G) and the liquid-phase mass transfer coefficient (k_L), typically expressed via the Sherwood number or the Ranz-Marshall correlation. While these methods offer computational efficiency and facilitate practical implementation, they tend to oversimplify complex multiphase interactions, especially at the reactive vapor-liquid interface. This simplification limits their predictive accuracy and the ability to design improved CO₂ absorption and reactive processes. Thus, they often fall short in delivering accurate predictions under varying solvents and operating conditions at the liquid-gas interface. As a result, the mechanisms governing CO₂ reactive mass transfer at the vapor-liquid interface remain insufficiently understood, emphasizing the necessity for more comprehensive and robust numerical models, as highlighted by several studies [13, 14].

1.2. Interfacial Reactive Mass Transfer Modeling

Numerical models for two-phase flow typically employ either sharp or diffuse interface approaches (DIM) to represent the interface between the two phases [15–17]. While sharp interface methods rely on abrupt property transitions, they are constrained by the resolution of the numerical mesh. In contrast, diffuse interface methods allow for smoother phase transitions, providing greater flexibility in modeling complex two-phase flow dynamics [15, 16]. For the present study, we adopt a DIM, which is better suited for analyzing complex interfacial reactive mass transfer processes. Among the various DIMs, the fully non-equilibrium seven-equation model provides the most detailed description of two-phase flow by accounting for individual pressures, velocities, and temperatures in each phase [18, 19]. However, its complexity and high computational cost limit its practical application [19, 20]. In contrast,

models that assume mechanical, kinetic, and thermal equilibrium simplify the governing equations by enforcing a single shared velocity, pressure, and temperature across phases, while allowing for nonequilibrium as a kinetically controlled process [21, 22]. These models capture species transport using two scalar equations, along with single-scalar equations for momentum and enthalpy, achieving a balance between computational efficiency and accuracy in describing reactive mass transfer dynamics. These two scalar equations for species transport in each phase are robust for high diffusivity ratios ($D_{\text{CO}_2(\text{g})}/D_{\text{CO}_2(\text{l})} \approx 10^4$), preventing unphysical mass leakage [21]. The system is closed by solving an interface equation, in this case, the phase-field equation, which models the dynamics of the phase boundary. A key challenge in these models is the accurate representation of scalar fluxes across phases. The complexity stems from integrating multiphase dynamics with thermodynamic principles and chemical reactions [22, 23]. While traditional Euler–Lagrange models treat droplets as point particles and rely on tunable parameters or simplified sub-models for interfacial mass transfer, phase change, and reaction, they often neglect interfacial dynamics, impose idealized vapor–liquid equilibrium (VLE), and omit kinetic complexity. In contrast, the present study adopts the diffuse-interface framework developed by [16, 24], which directly resolves interfacial dynamics through a two-scalar species transport model. Mass transfer is governed by relaxation to chemical equilibrium at the interface, allowing the model to capture non-ideal thermodynamic and kinetic effects often neglected in traditional approaches. A common simplification in prior work is the use of a constant Henry’s law coefficient [16, 24]; however, for reactive systems, it is essential to incorporate a temperature- and mole fraction-dependent coefficient to accurately represent the nonlinear vapor–liquid equilibrium during chemical reactions. Incorporating such a coefficient facilitates a more robust coupling between interface fluxes and the transport of reactive species, thermodynamic properties, and enthalpy. Another challenge is addressing velocity discontinuities at the reactive interface. While often neglected in multiphase models, recent studies underscore their importance in improving the fidelity of interfacial flow predictions [17, 25].

1.3. Contributions

This study presents a diffuse-interface model for mass and heat transfer between liquid and vapor, capturing chemical reactions. It employs a two-scalar species transport framework and proposes a novel formulation of the equilibrium-based approach for interfacial reactive mass transfer, ensuring consistent transitions between liquid-to-vapor and vapor-to-liquid phases. To account for non-ideal VLE effects, the model incorporates a locally varying apparent Henry’s constant, maintaining thermodynamic consistency in phase interactions. Additionally, the model includes interfacial reactive velocity discontinuities, which are often overlooked in traditional models. Simulations at the droplet scale are conducted with this new model, focusing on CO_2 capture in aqueous MDEA (Methyldiethanolamine) solvent systems. MDEA has been chosen for this study due to its high selectivity, chemical stability, low corrosiveness, and minimal regeneration energy requirements, which make it a preferred solvent for CO_2 capture processes [26, 27]. The simulations are designed to replicate real operating conditions, capturing the exchange of CO_2 and H_2O across the interface. The small-scale nature of this study allows for a detailed examination of CO_2 interfacial reversible reactive mass transfer, a phenomenon that remains underexplored due to scarce experimental data and the limited development of advanced numerical models at this scale.

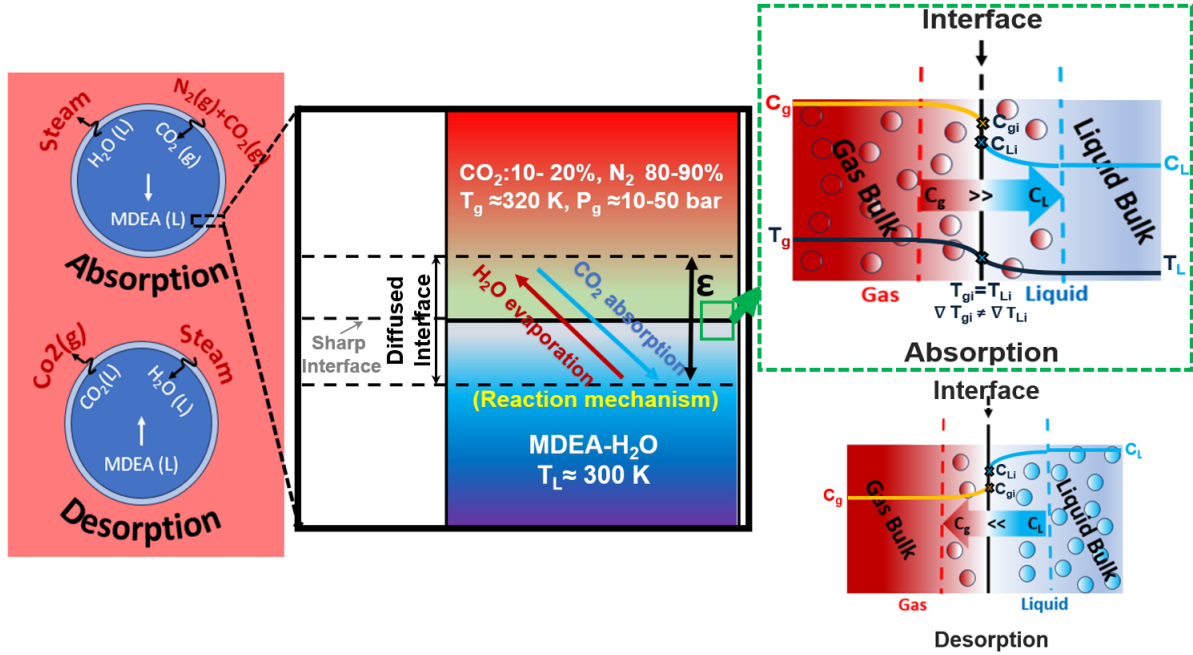


Figure 1: Interfacial CO_2 capture at the droplet scale

1.4. Research questions

Building on this modeling framework, the present study seeks to address the following key questions: How do solvent composition and ambient CO_2 concentration influence the interplay between interfacial mass transfer, reaction kinetics, and thermodynamic equilibrium during droplet-scale absorption and desorption? What roles do CO_2 and H_2O phase transitions—specifically, evaporation during absorption and condensation during desorption—play in modulating interfacial transport dynamics and reactive Stefan velocities across varying thermochemical regimes? Finally, how do multi-droplet configurations influence interfacial CO_2 absorption dynamics under different droplet numbers and imposed gas-phase flow conditions?

2. Mathematical Model

A mathematically consistent and physically valid model is required to describe the interfacial transport phenomena governing CO_2 capture at the droplet scale, as shown in Fig. 1. The following assumptions have been considered in this model.

- The gas phase is assumed to behave as an ideal gas, which is valid under ambient conditions of low temperature and pressure, typically encountered in CO_2 capture processes.
- Constant thermal and transport properties are assumed for individual components in the gas and liquid phases, due to the limited variation in pressure.
- The properties of the liquid, gas, and two-phase mixtures are computed using a linear mixing rule that incorporates the composition and phase fractions of the individual components, as detailed in the following subsections.

- At the droplet interface, thermo-chemical equilibrium is assumed, and the calculation of the equilibrium concentration for both gas and liquid is performed using a locally variable Henry's constant.
- All reactions take exclusively place in the liquid phase.
- Gravity effects are neglected, and an incompressible solver is employed.

2.1. Phase Field Equation

To track the interface between a multicomponent gas and a liquid, the phase field model introduced by [28] is used. The phase field parameter ϕ indicates the phases and the diffuse interface region, where $\phi = 1$ for the liquid, $\phi = 0$ for the gas, and intermediate values ($0 < \phi < 1$) represent the interface region.

The evolution of the interface is governed by

$$\frac{\partial \phi}{\partial t} + \nabla \cdot (u_\Gamma \phi) = \nabla \cdot \left\{ \Gamma \left[\epsilon \nabla \phi - \frac{1}{4} \left(1 - \tanh^2 \left(\frac{\psi}{2\epsilon} \right) \right) (\nabla \psi / |\nabla \psi|) \right] \right\} \quad (1a)$$

$$\psi = \epsilon \ln \left(\frac{\phi + \epsilon_0}{1 - \phi + \epsilon_0} \right) \rightarrow \epsilon_0 \approx 10^{-16}, \epsilon = \Delta x \quad (1b)$$

where the divergence term on the right-hand side of the equation is used to avoid artificial numerical diffusion of the interface thickness; the coefficient ϵ determines the thickness of the interface and is assumed to be approximately close to the mesh size. The function ψ represents the signed-distance from the interface, as described in Equation (1b). The choice of Γ is essential to ensure that the transport of ϕ remains constrained between 0 and 1. As proposed by [28], Γ is determined by calculating the maximum absolute velocity within the domain. Additionally, u_Γ represents the velocity of the non-divergence-free interface, used in the advection term, as detailed later.

2.2. Scalar Transport Modeling

2.2.1. Two-Scalar Transport for Concentration

Given the focus on individual species behavior, including phase transitions and chemical reactions, we employ two-scalar transport equations in molar concentration form for the liquid and gas phases [16, 24], as given in Equations 2-3.

$$\frac{\partial c_{1,i}}{\partial t} + \nabla \cdot (\vec{u} c_{1,i}) = \nabla \cdot \left[D_{1,i} \left(\nabla c_{1,i} - \left(\frac{1 - \phi}{\epsilon} \right) \vec{n} c_{1,i} \right) \right] + S_{12,i} + R_{1,i} \quad (2)$$

$$\frac{\partial c_{2,i}}{\partial t} + \nabla \cdot (\vec{u} c_{2,i}) = \nabla \cdot \left[D_{2,i} \left(\nabla c_{2,i} + \frac{\phi}{\epsilon} \vec{n} c_{2,i} \right) \right] - S_{12,i} \quad (3)$$

Where indices 1 and 2 correspond to the liquid and gas phases, i represents the species index within each phase, and $\vec{n} = \frac{\nabla \phi}{|\nabla \phi|}$ is the unit vector normal to the interface. The concentration c is expressed in mol/m³, and D denotes the diffusion coefficient (m²/s). The term S_{12} represents the interfacial mass transfer between the phases, while R_1 is the reaction source term in the liquid phase. The form of the diffusion (divergence term) is such to ensure the scalar is confined to one phase and ensures consistent transport of scalar and interface [24].

2.2.1.1 Multicomponent Interfacial Mass Transfer Mechanism.

The interfacial mass transfer term, $S_{12,i}$, in Equations 2-3 represents the net flux of species i from phase 2 (gas) to phase 1 (liquid). The fluxes liquid-to-gas and gas-to-liquid must balance, $S_{12,i} + S_{21,i} = 0$ for each species i . This condition reflects mass conservation. The interfacial transfer term for species i is given by Equation 4.

$$S_{12,i} = AD_{12,i} [E_{12,i} c_{2,i} \phi - c_{1,i} (1 - \phi)] - D_{12,i} \nabla \phi \cdot \nabla (c_{1,i} + E_{12,i} c_{2,i}) \quad (4)$$

The mass flux $S_{12,i}$ is function of the concentrations ($c_{1,i}$, $c_{2,i}$) in both phases, the phase field parameter ϕ , the equilibrium concentration ratio $E_{12,i}$, and the interfacial diffusion coefficient $D_{12,i}$, reported in Equation 5 below. The parameter A represents the inverse time scale for thermodynamic equilibrium and is typically chosen as a large constant (e.g., $A = 1000$) without imposing additional time-step restrictions [24].

$$D_{12,i} = \frac{D_{1,i} D_{2,i}}{E_{12,i} D_{1,i} (1 - \phi) + D_{2,i} \phi} \quad (5)$$

The equilibrium concentration ratio, $E_{12,i}$, defines the phase equilibrium condition for a given species at the interface, see Equation 6. Our formulation accounts for both CO_2 mass transfer and water phase change, which occur simultaneously in the system.

$$E_{12,i} = \begin{cases} \frac{RT}{H_{\text{CO}_2}(T, X_{\text{MDEA}})} & \text{for } i = \text{CO}_2 \text{ (absorption/desorption)} \\ \frac{c_{1,\text{H}_2\text{O}}}{P_{\text{vap}}(Y_{2,\text{H}_2\text{O}}, T)} = \frac{c_{1,\text{H}_2\text{O}} RT}{Y_{2,\text{H}_2\text{O}} P_{\text{vap}}(T)} & \text{for } i = \text{H}_2\text{O} \text{ (evaporation/condensation)} \end{cases} \quad (6)$$

For CO_2 transport, the equilibrium ratio is governed by the apparent Henry's constant, $H_{\text{CO}_2}(T, X_{\text{MDEA}})$, which is temperature- and solvent (MDEA) composition-dependent. Here, X_{MDEA} represents the mole fraction of MDEA in the liquid phase. The effective thermodynamic behavior is governed by complex and computationally expensive principles such as VLE [20, 22]; nevertheless, the apparent Henry's constant provides a simplified, empirically derived approximation of the system's nonlinear behavior under local thermodynamic conditions. Although the apparent Henry's constant provides a less fundamental description, it effectively captures the underlying complexity of the system, making it a valid estimation for engineering applications, when compared to the more comprehensive VLE thermodynamic models. Therefore, the non-ideal behavior of H_{CO_2} , arising from solvent- CO_2 interactions and volatility effects under VLE conditions, necessitates the use of empirical or semi-empirical correlations, which influence the interfacial reactive mass transfer dynamics. In this context, the apparent Henry's constant, and the diffusion coefficients of CO_2 in the MDEA- H_2O mixture are taken from the studies in [5, 26], as summarized in Table 1. In this table, the parameter p_j , used for computing the Henry's constant and the diffusion coefficient of CO_2 at the interface, depends on the solvent mole fraction, as well as the p_{ji} values, provided in Table 2. The diffusion coefficients for the other species involved in the process in both phases, are listed in Table 3.

For water phase transitions, the equilibrium ratio is determined via Raoult's law, which assumes ideal gas behavior and is applicable under conditions of minimal water phase change.

Table 1: Apparent Henry and diffusion coefficients of dissolved CO_2 in the MDEA- H_2O system mixture, as reported in [5, 26].

Coefficient	Equation
Apparent Henry $H_{\text{CO}_2(12)}(T, X_{\text{MDEA}})$	$H = p_0 + \frac{p_1}{T} + \frac{p_2}{T^2}$
Diffusion $D_{\text{CO}_2(12)}(T, X_{\text{MDEA}})$	$D = p_3 + p_4 T + p_5 T^2$
Parameter $p_j(X_{\text{MDEA}})$	$p_j = p_{j1} + p_{j2} X_{\text{MDEA}} + p_{j3} X_{\text{MDEA}}^2 + p_{j4} X_{\text{MDEA}}^3$

Table 2: Coefficients for the rate coefficient equation presented in Table 1 [5, 26].

i/j	p_{ji}			
	1	2	3	4
0	2.01874	$-2.37668 * 10^1$	$2.90092 * 10^2$	$-4.80196 * 10^2$
1	$3.13549 * 10^3$	$1.54931 * 10^4$	$-1.83987 * 10^5$	$3.00562 * 10^5$
2	$-8.13702 * 10^5$	$-2.48081 * 10^6$	$2.92013 * 10^7$	$-4.70852 * 10^7$
3	$2.46851 * 10^{-4}$	$-1.00629 * 10^{-3}$	$2.87762 * 10^{-3}$	-
4	$-1.99813 * 10^{-6}$	$5.98956 * 10^{-6}$	$-1.73422 * 10^{-5}$	-
5	$4.13889 * 10^{-9}$	$-8.99012 * 10^{-9}$	$2.56824 * 10^{-8}$	-

Table 3: Diffusion Coefficient of Different Species in the Two-Phase System [29, 30]

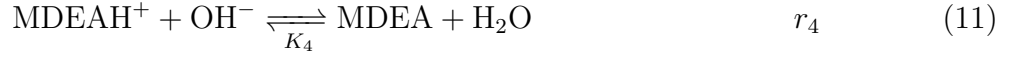
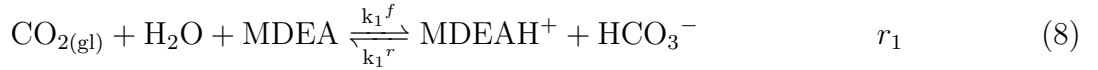
Phase	Species	$D \times 10^{-9} [\text{m}^2/\text{s}]$	Phase	Species	$D \times 10^{-6} [\text{m}^2/\text{s}]$
Liquid	MDEA	0.848	Vapor	Steam	25
	MDEAH^+	5.01		CO_2	15
	HCO_3^-	1.18			
	OH^-	5.2			
	CO_3^{2-}	1.01			

Here, $c_{1,\text{H}_2\text{O}}$ represents the concentration of water in the liquid phase, while $Y_{2,\text{H}_2\text{O}}$ denotes the molar fraction of water in the gas phase. Additionally, $P_{\text{vap}}(T)$, measured in kPa, corresponds to the equilibrium vapor pressure of water at temperature T . The water vapor pressure is calculated using Tetens equation [31], which provides an empirical relationship for the saturation pressure:

$$P_{\text{vap}} = 0.61078 \exp \left(\frac{17.27(T - 273)}{(T - 273) + 237.3} \right) \quad (7)$$

2.2.1.2 Chemical reaction mechanism.

To capture the CO_2 reactive mass transfer dynamics, an additional source term, $R_{1,i}$, is incorporated into the liquid phase equation, as shown in Equation 2. This term, present for the species involved in the reaction process, is crucial for a correct kinetic modeling. Among the various models proposed in the literature [30], we have selected the mechanism outlined below in Equations 8 to 11; this is supported by numerous studies [5, 27, 32].



This model accounts for reversible reactions and incorporates thermochemical correlations [26, 33, 34]. The general expression for the reaction rates \dot{r}_j in each reaction j is given by [34, 35]:

$$\dot{r}_j = \left(k_j^f \prod_{i \in \text{react}} [c_i]^{-\nu_{ij}} \right) - \left(k_j^r \prod_{i \in \text{prod}} [c_i]^{\nu_{ij}} \right) \quad (12)$$

In this context, k_j^f , k_j^r , and K_j denote the forward, reverse, and equilibrium rate constants, respectively, where the reverse reaction rate, k_j^r , is related to the equilibrium constant by $k_j^r = \frac{k_j^f}{K_j}$. The stoichiometric coefficients, ν_{ij} , are negative for reactants and positive for products. The concentration variations over time of each species in equation (2) are governed by the mass action law [34], with the corresponding reaction rates \dot{r}_j shown in Equation (13).

$$R_i = \sum_j \nu_{ij} \dot{r}_j \quad (13)$$

According to [5, 27, 36], reactions (8) and (9) proceed at finite rates, while reactions (10) and (11) occur instantaneously, involving only proton transfer. Therefore, the OH^- and CO_3^{2-} species should be modeled according to

$$\begin{aligned} c_{\text{OH}^-} &= \frac{1}{K_4} \frac{c_{\text{MDEA}}}{c_{\text{MDEAH}}} \\ c_{\text{CO}_3^{2-}} &= \frac{K_3}{K_4} \frac{c_{\text{MDEA}} c_{\text{HCO}_3^-}}{c_{\text{MDEAH}}}. \end{aligned} \quad (14)$$

For each reaction, various correlations have been proposed to calculate the forward rate constant (k_j) and the equilibrium constant (K_j), with temperature as the key variable [30]. The kinetic parameters adopted here for the CO₂-MDEA-H₂O system are obtained from experimental correlations as detailed in [5, 27]; the resulting expressions are summarized in Table 4. Note finally that, due to the presence of multiple components in both phases, one does

Table 4: Kinetic parameters for the CO₂-MDEA-H₂O system [5, 27].

Reaction	Equation	T(K) range
r_1	$k_1 = 4.01 \times 10^8 \exp\left(-\frac{5400}{T}\right)$	293-353
	$\log(K_1) = 77.404 - \frac{1967}{T} - 27.999 \log(T) + 2.9116 \times 10^{-2}T$	293-383
r_2	$\log(k_2) = 13.635 - \frac{2895}{T}$	293-383
	$\log(K_2) = 115.36 - \frac{5652.1}{T} - 41.882 \log(T) + 2.9116 \times 10^{-3}T - \log(K_w)$	293-383
r_3	$\log(K_3) = 95.5739 - \frac{5399.02}{T} - 35.4819 \log(T) - \log(K_w)$	293-383
r_4	$\log(K_4) = 37.956 - \frac{3684.5}{T} - 13.833 \log(T) - \log(K_w)$	293-383
Water Dissociation	$\log(K_w) = 8909.483 - \frac{142613.6}{T} - 4229.195 \log(T)$ $+9.7384T + 1.29638 \times 10^{-2}T^2 + 1.15068 \times 10^{-5}T^3 - 4.602 \times 10^{-9}T^4$	293-383

not need to solve for all species transport. The concentrations of specific species—namely, nitrogen in the gas phase and water in the liquid phase—are determined using mass balance and mole fraction constraints, that is $X_{N_k} = 1 - \sum_{i=1}^{N_k-1} X_i$ for the liquid phase and $Y_{N_k} = 1 - \sum_{i=1}^{N_k-1} Y_i$ for the gas phase, where N_k denotes the total number of species in phase k . This ensures consistency with the overall mass conservation of the system.

2.2.2. Conservation of energy: Transport of Enthalpy

To ensure the conservation of energy during interfacial reactive mass transfer, the temperature distribution is described by the following single-scalar enthalpy equation, where *single scalar* is used to indicate that one single value of the temperature is assumed, also in the mixed zone where the two phases coexist.

$$\frac{\partial \rho h}{\partial t} + \nabla \cdot (\vec{u} \rho h) = \nabla \cdot (k \nabla T) + h_{rxn} - \dot{m}_\Gamma h_{lv} \delta_\Gamma \quad (15)$$

In the above, ρ denotes mixture density, k thermal conductivity, $h = c_p T$ is specific enthalpy (with temperature T and specific heat capacity c_p), and h_{lv} represents latent heat for phase transitions. Mixture properties are calculated as

$$\alpha = \sum_{i=1}^{N_l} (\alpha_i^l \cdot Y_i^l \cdot \phi) + \sum_{i=1}^{N_g} (\alpha_i^g \cdot Y_i^g \cdot (1 - \phi)),$$

which represents a linear combination of contributions from species in both the liquid and gas phases, with α_i^l and α_i^g the respective properties of species i in the liquid ($k = l$) and gas ($k = g$) phases, Y_i^k the molar fractions, and ϕ the phase field parameter. N_l and N_g represent the total number of species in the liquid and gas phases, respectively. Due to the lack of experimental data for ionic properties, the liquid-phase properties are estimated based on the mixing behavior of the reactants, which is considered a reasonable approach for dilution studies [35]. The property values are obtained from published sources and are summarized in Table 5 [5, 26, 30]. The latent heat of vaporization, h_{lv} , of water is assumed to be 2000 kJ/kg.

Table 5: Thermophysical Properties of the System [5, 26, 30]

Phase	Species	ρ [kg/m ³]	μ [kg/(m·s)]	c_p [J/(kg·K)]	κ [W/(m·K)]	M_W [kg/mol]
Liquid($T_l=300\text{K}$)	H ₂ O	997	0.000547	4179	0.684	0.018015
	CO ₂	1087.18	0.000073	847	0.162	0.04401
	MDEA	1039	0.000672	3870	0.052	0.119163
Gas($T_g=320\text{K}$)	N ₂	1.178	0.0000187	1040	0.0258	0.0280124
	CO ₂	1.877	0.000015	660	0.016	0.04401
	H ₂ O	1.202	0.00002	1872	0.024	0.018015

Table 6: Standard Heat of Formation for Various Species in the [30, 37]

Phase	Species	Δh_f° (kJ/mol)	Phase	Species	Δh_f° (kJ/mol)
Liquid	Water	-285.8	Vapor	Steam	-241.8
	MDEA	-445.58		N ₂	0
	CO ₂ (aq)	-420.5		CO ₂ (g)	-393.5
	MDEAH ⁺	-80			
	HCO ₃ ⁻	-691.1			
	OH ⁻	-228.1			
	CO ₃ ²⁻	-676.3			

The heat reaction rate h_{rxn} is calculated using Equation (16), which involves the product species and reactants:

$$h_{\text{rxn}} = - \sum_j \dot{r}_j \left(\sum_{i \in \text{prod}} \nu_{ij} \Delta h_{f,i}^\circ - \sum_{i \in \text{react}} \nu_{ij} \Delta h_{f,i}^\circ \right) \quad (16)$$

The reaction rates \dot{r}_j in each reaction j (Eq.'s (8) to (11)) are computed using Eq. (12). The term $\Delta h_{f,i}^\circ$ refers to the standard enthalpies of formation for the products and reactants, with their values provided in Table 6 [30, 37].

2.2.3. Transport of Momentum and Mass Conservation

We solve the momentum equations using a conventional pressure correction method, as detailed in [16, 17]. The momentum equation is given by:

$$\frac{\partial(\rho \vec{u})}{\partial t} + \nabla \cdot (\vec{u}(\rho \vec{u})) = -\nabla \mathbf{P} + \nabla \cdot [\mu (\nabla \vec{u} + (\nabla \vec{u})^\top)] \quad (17)$$

We can resort to the pressure correction method via the following steps:

$$\frac{\vec{u}^{**} - \vec{u}^n}{\Delta t^{n+1}} = f_{t,1} \mathbf{R}^n + f_{t,2} \mathbf{R}^{n-1} \quad (18)$$

$$\vec{u}^* = \vec{u}^{**} - \frac{\Delta t^{n+1}}{\rho_0^{n+1}} \left[\left(1 - \frac{\rho_0}{\rho^{n+1}} \right) \nabla \hat{p} + \nabla p^n \right] \quad (19)$$

$$\nabla^2 \delta p^{n+1} = \frac{\rho_0^{n+1}}{\Delta t} (\nabla \cdot \vec{u}^* - \nabla \cdot \vec{u}_\Gamma) \quad (20)$$

$$p^{n+1} = p^n + \delta p^{n+1} \quad (21)$$

$$\vec{u}^{n+1} = \vec{u}^* - \frac{\Delta t^{n+1}}{\rho_0} \nabla \delta p^{n+1} \quad (22)$$

The interfacial velocity is computed using a strategy [17, 38], specifically applied to a sharp interface approach. For the present study, this method is extended to a diffuse interface, incorporating the velocity jump (Stefan flow) into the gas domain. The velocity jump arises due to mass transfer driven by differences in molar density between the phases (where mass density $\rho_i = c_i \cdot M_{w,i}$), and it satisfies the principle of mass conservation. For comprehensive details, we refer to [17, 39]. Thus, considering the mass balance between the phases, the non-zero velocity divergence can be expressed as:

$$\nabla \cdot \vec{u}_\Gamma = \dot{m}_\Gamma \left(\frac{1}{\rho_{g,\Gamma}} - \frac{1}{\rho_{l,\Gamma}} \right) \delta_\Gamma \quad (23)$$

where $\delta_\Gamma = \nabla \phi \cdot \vec{n}_\Gamma$ is the Dirac delta function, and \vec{n}_Γ is the interface normal vector. The mass transfer between the phases is governed by the interfacial concentration gradients of all species [40, 41].

$$\dot{m}_\Gamma = \sum_{i=1}^n \dot{m}_{12}^i = - \sum_{i=1}^n D_{12}^i \nabla c_{12}^i M_{w,i} \vec{n}_\Gamma \quad (24)$$

Here, D_{12}^i represents the interfacial diffusion coefficient (see Eq. (5)), $M_{w,i}$ is the molecular weight, and ∇c_{12}^i denotes the concentration gradient at the interface, calculated through the scalar equations, for species i .

2.3. Numerical implementation

The governing equations are discretized on a uniform Cartesian grid with spacing $\Delta x = l_x/N_x$, where l_x is the domain length and N_x is the number of grid cells in the x -direction, with analogous definitions for y and z . A finite-volume discretization is implemented on a staggered grid. Scalar quantities, including the phase field, pressure, and transport properties, are stored at cell centers, while velocity components are defined at cell faces to enhance numerical stability and ensure accurate flux evaluations. To solve the Navier-Stokes equations, we adopt a projection method combined with a pressure-splitting technique [42]. Time integration is performed using the second-order Adams-Bashforth scheme, while spatial derivatives are discretized with a second-order central difference scheme for improved accuracy. More details can be found in [43].

Table 7: Geometry configuration for different scenarios with varying number and size of droplets (all in mm). x_c , y_c , and z_c denote the coordinates of the droplet center, r_c is the droplet radius, and L_b , n_{L_i} , and Δx_i indicate the box length, the number of grid points, and the mesh size along each axis.

Droplet numbers	z_c	y_c	x_c	r_c	L_b	n_{L_i}	Δx_i
Single	0	0	0	0.2	1.5	256	0.006
	-1	-1	0	0.1			
Two					3	375	0.008
	1	1	0	0.1			
	-1	-1	0	0.1			
Four					3	375	0.008
	1	1	0	0.1			
	-1	1	0	0.1			
	1	-1	0	0.1			

3. Model Setup

We investigate how solvent composition, a key factor in CO_2 absorption, influences the interplay between interfacial mass transfer and chemical reactions in CO_2 capture systems using the diffusive two-scalar transport framework. From a classical thermodynamic perspective, CO_2 absorption occurs when its gas phase concentration ($c_{\text{CO}_2(g)}$) exceeds that of the liquid phase ($c_{\text{CO}_2(l)}$), while desorption occurs when the gas phase concentration is lower than that of the liquid phase concentration, as depicted in Fig. 1. As highlighted by [44], large, non-spherical droplets can exhibit internal flows. However, for smaller droplets (typically below 1 mm in diameter), such effects are negligible [45]. Therefore, the analysis begins with a single-droplet configuration and is subsequently extended to multi-droplet scenarios, with geometric parameters and numerical resolution summarized in Table 7.

A set of boundary conditions is applied to the computational domain. Periodic boundary conditions are chosen for parameters related to mass transfer, chemical reactions, and enthalpy. Neumann and Dirichlet boundary conditions are employed for the velocity and pressure distributions in the pressure-velocity coupling process.

In all cases, the ambient and liquid droplet temperatures are assumed constant: $T_l = 300\text{ K}$ and $T_g = 320\text{ K}$, respectively. Two distinct sets of initialization conditions are defined for the absorption and desorption cases, derived from the corresponding operational parameters and thermophysical properties listed in Table 8 and Table 5, respectively.

Parameter	Absorption Case	Desorption Case
Liquid Species	H_2O , MDEA (X_{MDEA} 0–0.30)	H_2O , CO_2 , (X_{MDEA} : 0–0.30)
Gas Species (inlet)	N_2 , CO_2 ($Y_{\text{CO}_2} = 0.10$)	H_2O (Steam)
Liquid Temperature [K]	300	300
Gas Temperature [K]	320	320
Operating Pressure	Atmospheric	Atmospheric
Thermophysical Properties	Table 5	Table 5

Table 8: Initialization for absorption and desorption simulations.

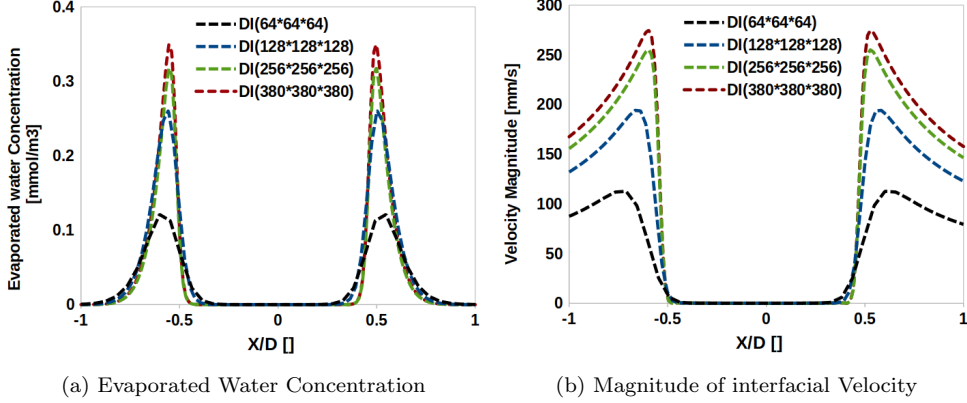


Figure 2: Grid resolution analysis showing the water evaporation concentration (a) and the magnitude of the reactive stefan velocity (b) during the CO_2 absorption, with results presented for varying grid resolutions (64, 128, 256, and 380 points along each axis). The data are plotted along the centerline axis for a single droplet.

3.1. Grid-Resolution Sensitivity Analysis

A sensitivity analysis is initially conducted for a single droplet to evaluate the impact of grid-resolution on the computational results. Simulations are performed with grid resolutions of 64, 128, 256, and 380 (≈ 55 million cells) grid points in each direction. The analysis focuses on water evaporation concentration (which has a higher diffusion coefficient than the liquid) and interfacial velocity magnitude during CO_2 absorption, as shown in Fig. 2. The results indicate that lower grid resolutions introduce excessive diffusion, leading to an underestimation of key parameters, while higher resolutions exhibit convergence, thereby confirming the numerical approach's grid independence.

4. Results and Discussion

4.1. Thermodynamic Insights into CO_2 Absorption in Aqueous MDEA Solutions

The dynamics of interfacial reactive mass transfer are governed by the apparent Henry's constant, diffusion coefficients, and phase concentration gradients. An analysis of the thermodynamic factors offers key insights into the mass-transfer mechanisms.

Figure 3 illustrates the distribution of the apparent Henry constant (*a*) and the interfacial diffusion coefficient (*b*) for CO_2 in the *MDEA + H₂O* mixture across various temperatures and MDEA solvent compositions (mole fraction). In the operational range typically used for CO_2 absorption, Henry's constant varies by a factor of approximately 6, indicating strong temperature sensitivity of solubility, while the diffusion coefficient changes by a factor of about 7-10, significantly affecting species transport. The results further indicate that increasing the MDEA mole fraction elevates the apparent Henry constant, whereas it reduces the interfacial diffusion coefficient, thereby limiting molecular mobility within the liquid phase. These variations have a substantial impact on the driving force and mass flux, underscoring the importance of incorporating temperature- and composition-dependent properties into the interfacial scalar transport model.

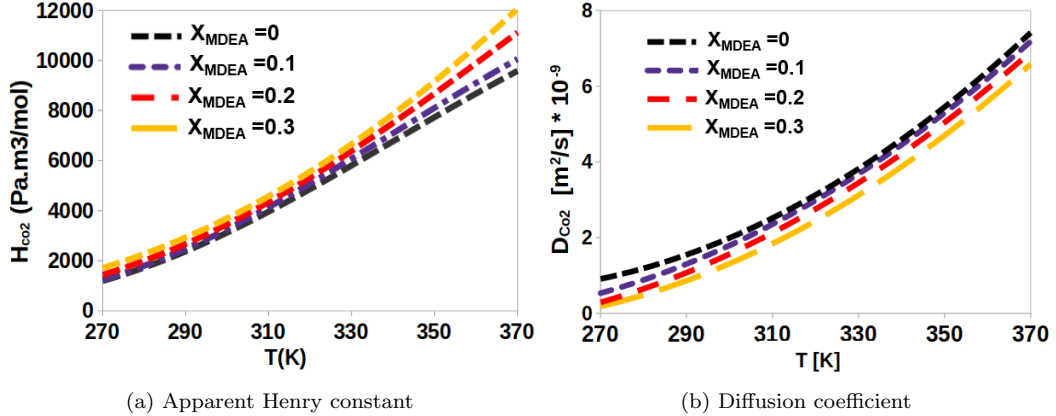


Figure 3: Apparent Henry constant coefficient [$\text{Pa}\cdot\text{m}^3/\text{mol}$] (a) and Diffusion coefficient [m^2/s] $\times 10^{-9}$ (b) of CO_2 in the $MDEA + H_2O$ mixture for various MDEA mole fractions.

4.2. Interfacial Mass Transfer Mechanisms in CO_2 Capture

The proposed two-scalar model provides an integrated framework that inherently captures both absorption and desorption processes, depending on the operating conditions. Absorption–desorption dynamics are governed by concentration gradients and interfacial resistance. A negative S_{21} ($c_{CO_2,g} > c_{CO_2,l}$) drives absorption, while a positive S_{21} triggers desorption. Interfacial resistance arises from non-ideal VLE behavior, influenced by the apparent Henry’s constant, interfacial diffusivity, temperature, and solvent properties, collectively determining the mass transfer direction and rate. Consequently, this interplay gives rise to distinct thermophysical behaviors in the carbon capture mechanism, as illustrated in Fig. 4. During absorption, solvent interaction induces water evaporation, while desorption leads to steam condensation around the gas. As illustrated in Fig. 4(a), the elevated CO_2 concentration in the gas phase promotes the transfer of CO_2 to the liquid phase, as illustrated by velocity vector contours (commonly referred to as Stefan flow in non-reactive systems). This inter-

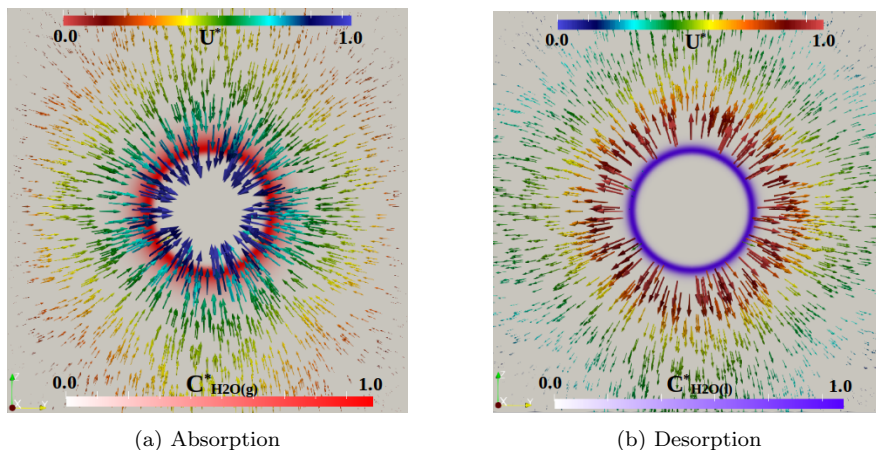


Figure 4: Thermophysical behavior during CO_2 absorption and desorption. (a) Absorption: High CO_2 concentration in the gas phase drives CO_2 transfer to the liquid, with water evaporation indicated by the red contour. (b) Desorption: Higher CO_2 concentration in the liquid promotes CO_2 release to the gas phase, leading to steam condensation around the droplet, shown by the blue contour.

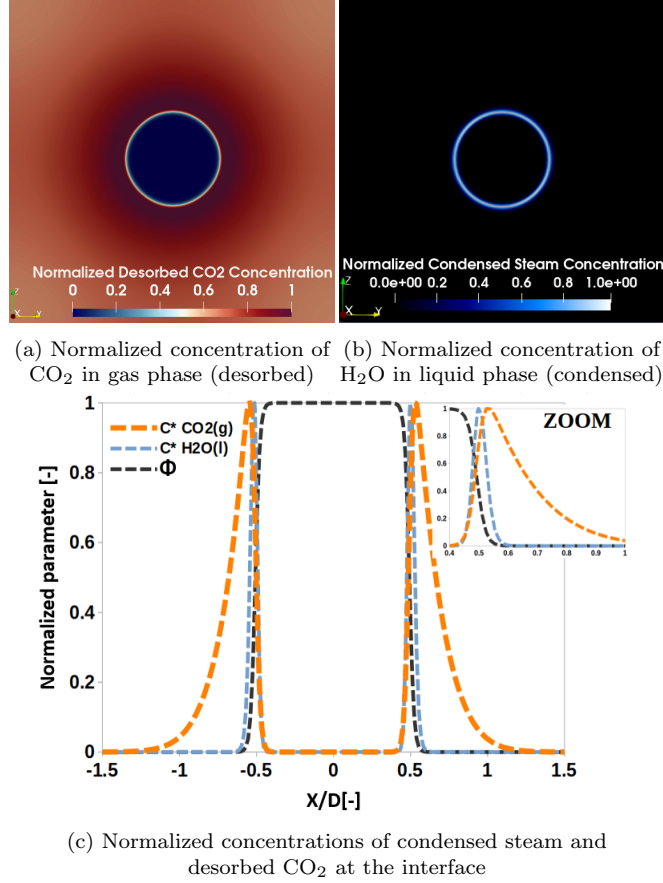


Figure 5: Contours of normalized desorbed CO_2 concentration (a) and condensed steam (H_2O) concentration (b), along with their profiles (c), normalized to the maximum values at the specified time step for both CO_2 and H_2O , $X_{\text{MDEA}} = 0.3$, at $t = 10$ ms. The influence of the gas-phase and liquid-phase diffusion coefficients is evident in the spatial distribution of these species, reflecting the differential rates of mass transfer and the development of concentration gradients across the phases.

action between CO_2 and the aqueous medium induces chemical reactions, leading to tiny water evaporation, which is represented by the red contours in the gas phase, around the droplet. Conversely, during desorption, the higher concentration of CO_2 in the liquid phase drives the release of CO_2 from the liquid to the gas phase, as shown by the velocity contour plots. This process simultaneously facilitates the condensation of steam around the droplet, as indicated by the blue contours representing water.

Fig. 5 presents the contours of normalized desorbed CO_2 (a) and condensed steam concentrations (b) after $t = 10$ ms. The concentrations are normalized by their maximum values at the specified time step. The distinct dynamics of CO_2 desorption and steam condensation arise from the different diffusivities of gases and liquids. CO_2 in the gas phase exhibits rapid dispersion throughout the domain due to its higher diffusivity, whereas condensation generates steep concentration gradients confined to narrow regions, governed by the lower diffusivity in the liquid phase. This results in a desorption peak near the gas-side interface ($0 < \phi < 0.5$), with maximum condensation near the liquid side ($0.5 < \phi < 1$), as shown in (c). From the first simulation time step, each cell represents a diffuse interface, with the

phase field parameter ranging from 0 to 1 ($0 < \phi < 1$), and the concentration distribution evolves over time.

Similar interfacial mechanisms govern the absorption–evaporation process. In the CO_2 absorption scenario, low liquid-phase diffusivity ($\approx 10^{-9}$) hinders mass transfer, extends interfacial residence time, and increases sensitivity to local concentration gradients [46].

4.3. Effect of MDEA Solvent on the Temporal Dynamics of Interfacial CO_2 Absorption

Optimizing interfacial reactive CO_2 capture demands a fundamental understanding of solvent behavior, as it dictates absorption dynamics, efficiency, and contributes significantly to industrial costs. In particular, MDEA reshapes interfacial transport mechanisms, dynamically modulating absorption rates and driving multiscale transport phenomena. As illustrated in Figure 6, the temporal distributions of the reaction source term (a), and interfacial mass transfer source term (b) for CO_2 exhibit sensible variations across different MDEA mole fraction (X_{MDEA}). In the absence of MDEA ($X_{\text{MDEA}} = 0$), no reactions take place, leading to an optimized phase transfer. However, as MDEA mole fraction increases, the magnitude of mass transfer rate declines while reaction rates intensify. This behavior is attributed to the alteration of interfacial parameters, such as diffusion coefficients and the variable apparent Henry's constant, suggesting a self-regulating interaction between mass transfer and reaction kinetics. While the presence of MDEA solvent results in slower CO_2 mass transfer compared to water, it significantly enhances absorption capacity by chemically converting absorbed CO_2 into soluble species such as bicarbonate. This conversion continuously removes CO_2 from the gas–liquid interface, maintaining the concentration gradient that drives further absorption. As a result, the system achieves higher long-term CO_2 loading, absorption efficiency, and capacity—a behavior well established in packed bed systems and now demonstrated at the droplet scale[5, 26].

The absorption of CO_2 in the presence of an MDEA solvent exhibits multiscale dynamics, with mass transfer, diffusion, and chemical reaction processes operating on distinct time scales, as represented by specific terms in Equation 3. Consequently, a thorough understanding of interfacial reactive mass transfer requires an analysis of the contributions from various source terms, including diffusion (S_D), interfacial transfer (S_J), and reaction (S_R), corresponding to the first, second, and third terms on the right-hand side of equation 3,

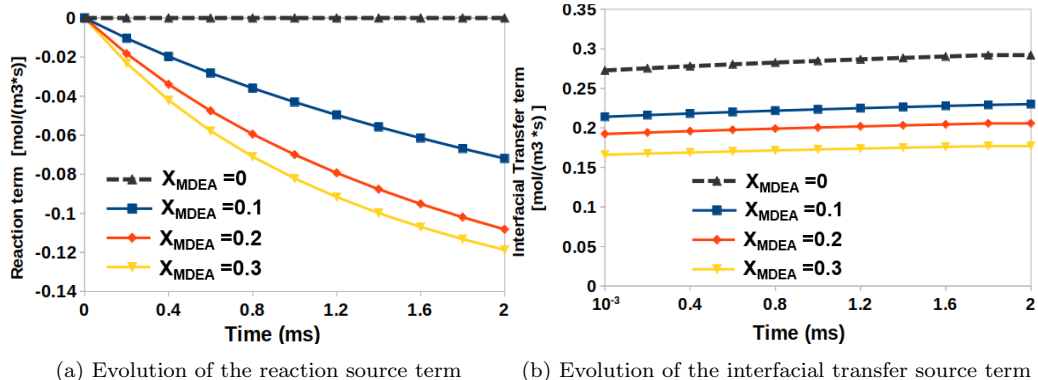


Figure 6: Temporal distribution of the reaction source term (a) and interfacial transfer source term (b) for CO_2 species across various MDEA mole fractions (X_{MDEA}).

respectively. These terms represent volumetric fluxes ($\text{mol m}^{-3} \text{s}^{-1}$) that quantify the local rate of CO_2 exchange associated with each underlying transport or reaction mechanism. Focusing on a fixed MDEA mole fraction of $X_{\text{MDEA}} = 0.1$, Fig. 7 illustrates the temporal evolution of these terms, highlighting their relative contributions. The interfacial transfer of

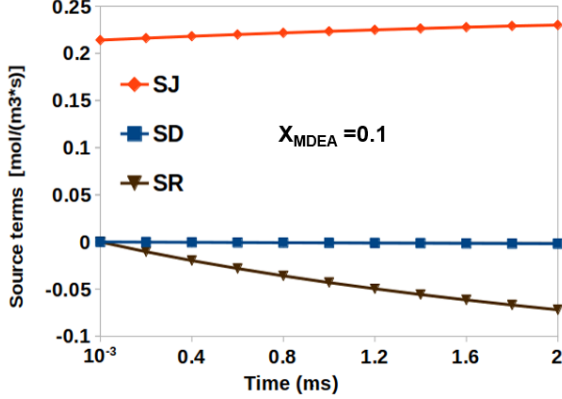


Figure 7: Evolution of various source terms for the CO_2 species with an initial composition of $X_{\text{MDEA}} = 0.1$. Here, S_J represents interfacial transfer, S_D denotes diffusion, and S_R corresponds to reaction source terms.

CO_2 , represented by S_J , occurs rapidly and dominates the early stages of the absorption process. In contrast, the diffusion (S_D) and reaction (S_R) processes evolve more gradually over time. Consequently, the interplay among these processes governs the overall CO_2 absorption mechanism, as seen in Figure 8, which presents the total source term (total volumetric flux). Therefore, it can be concluded that increasing MDEA mole fractions initially suppresses mass transfer but subsequently accelerates reaction kinetics, ultimately controlling the absorption process. By contrast, in the non-reactive case ($X_{\text{MDEA}} = 0$), the absence of the chemical reaction term S_R , as illustrated in Fig. 6(a), leads to a system governed exclusively by interfacial transfer and diffusion, resulting in simpler temporal dynamics. As a result, this comparison highlights the fundamental role of chemical reactions, encompassing kinetics and the associated mechanisms, in governing the multiscale characteristics of interfacial CO_2 absorption, distinguishing reactive systems from their non-reactive counterparts.

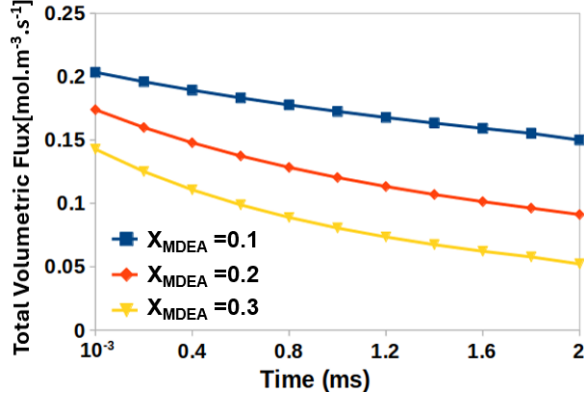


Figure 8: Temporal evolution of the total volumetric flux ($S_D + S_J + S_R$) for CO_2 across varying MDEA mole fractions (X_{MDEA}), highlighting the interplay between mass transfer and chemical reaction dynamics.

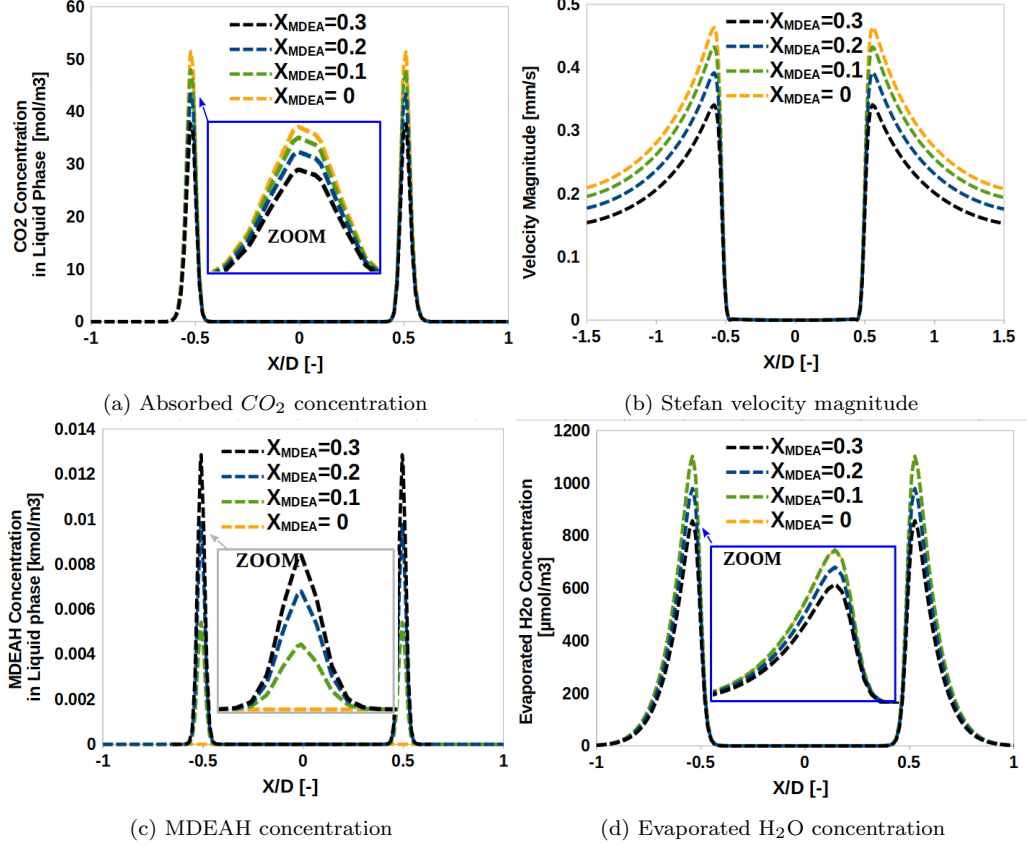


Figure 9: Spatial distribution of (a) Absorbed CO_2 concentration in the liquid phase, (b) Stefan velocity magnitude, (c) MDEAH concentration (provided as a representative species for the reaction products in the liquid phase), and (d) Evaporated H_2O concentration in the gas phase for different X_{MDEA} after $t = 100 \mu s$, along the droplet centerline axis.

4.4. Effect of MDEA Solvent on the Spatial Dynamics of Interfacial CO_2 Absorption

Fig. 9 illustrates the spatial distribution of key parameters: (a) absorbed CO_2 concentration in the liquid phase, (b) Stefan velocity magnitude, (c) MDEA concentration (representing a reaction product in the liquid phase), and (d) evaporated H_2O concentration in the gas phase, all evaluated at the central cut section of the droplet for varying X_{MDEA} . Additional results for the desorption process are provided in [Appendix A](#).

An increase in MDEA mole fraction suppresses CO_2 transfer, as shown in Fig. 9(a), resulting in lower absorbed concentrations. Concurrently, a higher solvent composition reduces mass flux and interfacial velocity magnitude, driven by interfacial reactive flow, as seen in Fig. 9(b). However, during the reaction phase, CO_2 interactions with MDEA generate various chemical products, with the reaction rate positively correlating with MDEA mole fraction, as shown in Fig. 9(c). Consequently, the mass transfer and reaction processes interact dynamically, with each influencing the other and adapting to prevailing system conditions. In addition, higher MDEA mole fractions lead to a reduction in water evaporation within the aqueous mixture, as illustrated in Fig. 9(d). This reduction is attributed to the modified properties and water content in the droplet, influenced by Raoult's law and changes in the vapor pressure of water. Notably, since temperature fluctuations remain minimal through-

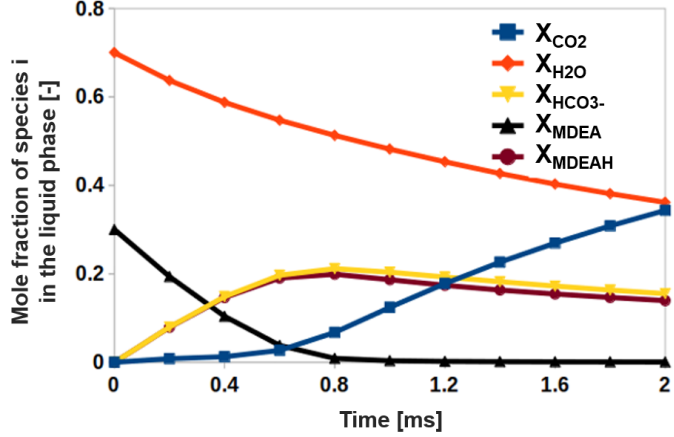


Figure 10: Temporal evolution of species mole fractions at the interface under conditions of $X_{MDEA(l)} = 0.3$, $Y_{CO_2(g)} = 0.2$

out the process, solvent composition becomes the dominant factor in governing evaporation, thereby controlling the evaporation rate and establishing it as the primary determinant. A similar trend is observed in the desorption case, as detailed in the appendix and illustrated for temperature in Figure A1(d). Despite the small magnitude of evaporated water, its contribution to reactive Stefan flow mechanism is negligible compared to that induced by CO_2 absorption. As a result, reactive Stefan flow is predominantly governed by CO_2 absorption rather than water evaporation, with the flow transitioning from the gas to the liquid phase, as shown in Fig. 4. These evaporation observations align with the study by [11] in different absorption applications.

Shedding light on the intricate interplay among different mechanisms as mass transfer, chemical reactions, and evaporation, Fig. 10 illustrates the temporal evolution of species mole fractions at the interface. This profile highlights the model's capability to characterize the generation, consumption, and evaporation processes of various species, including CO_2 , MDEA, MDEAH, HCO_3^- , and H_2O . The reaction between absorbed CO_2 and the MDEA solvent leads to the depletion of MDEA, subsequently generating protonated MDEAH $^+$ and bicarbonate ions (HCO_3^-), signifying the characteristic behavior of CO_2 absorption in amine-based solvents. This interplay between mass transfer and reaction kinetics results in the gradual rise of reaction products while simultaneously depleting the reactants. Simultaneously, a reduction in water mole fraction is observed due to the increasing formation of kinetic products in the liquid and water evaporation.

4.5. Gas-Phase CO_2 Concentration in the Absorption Mechanism

The gas-phase CO_2 concentration ($c_{CO_2(g)}$) significantly influences the dynamic behavior of the absorption dynamics. Figure 11 shows that increasing $c_{CO_2(g)}$ enhances CO_2 absorption and accelerates MDEA depletion, introducing distinctive nonlinear behaviors that vary with operational conditions. This underscores the significant role of gas-phase CO_2 concentration in shaping absorption efficiency and solvent utilization.

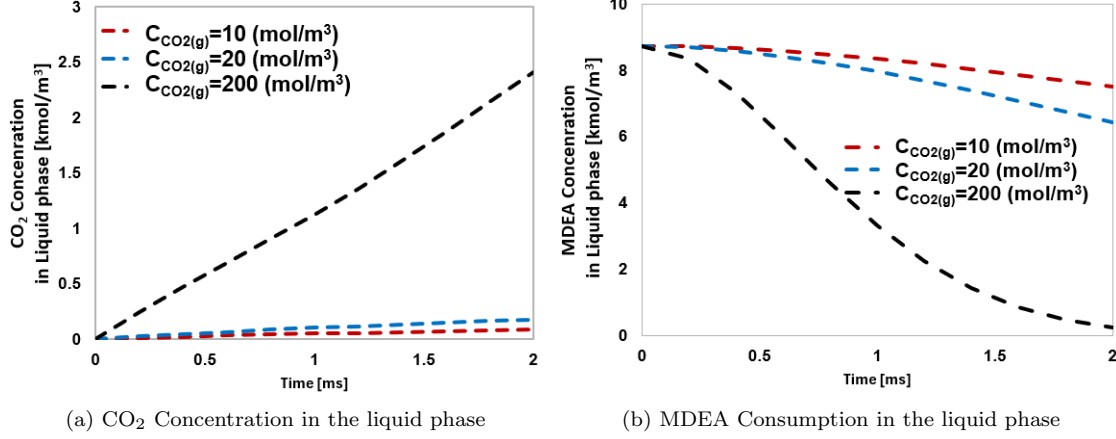


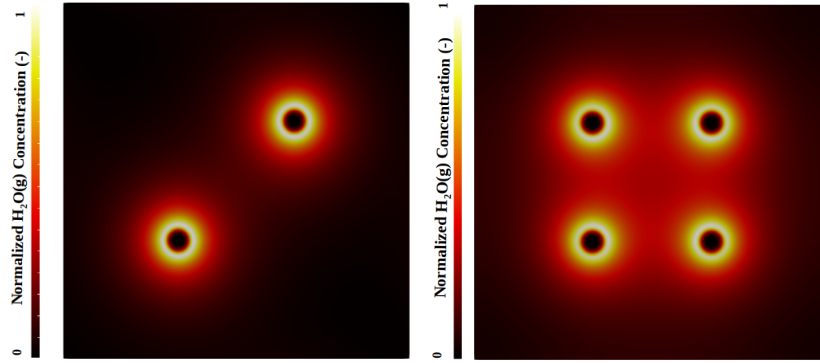
Figure 11: Temporal evolution of CO₂ concentration (a) and MDEA (b) in the liquid phase for varying initial $c_{CO_2(g)}$, with an initial MDEA mole fraction of $X_{MDEA,l} = 0.3$ at the liquid-gas interface.

4.6. Interfacial Reactive Dynamics in Multi-Droplet CO₂ Absorption Systems

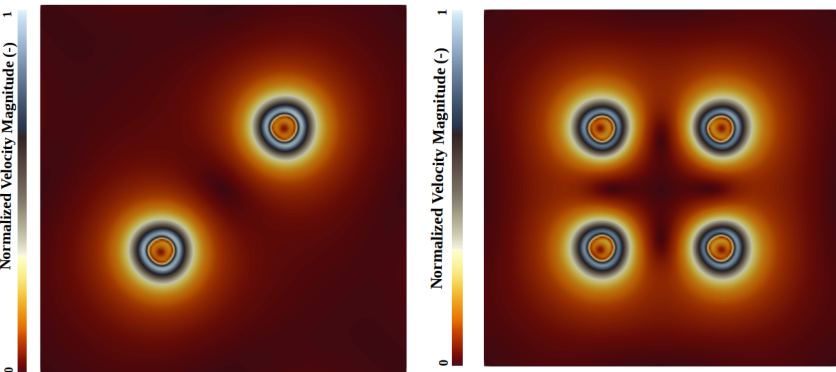
In industrial spray systems, CO₂ absorption is influenced by the intricate dynamics of multiple droplets and their interactions with the surrounding environment. We therefore investigate CO₂ absorption under two distinct flow regimes: (i) reactive Stefan flow in the absence of an imposed gas-phase mean flow, and (ii) reactive Stefan flow in the presence of a constant mean flow. These conditions are examined across two geometric configurations—comprising two and four droplets—as summarized in Table 7, to evaluate the combined influence of flow regime and geometry on the absorption dynamics.

4.6.1. Effect of Droplet Number on Reactive CO₂ Absorption under No Mean Flow

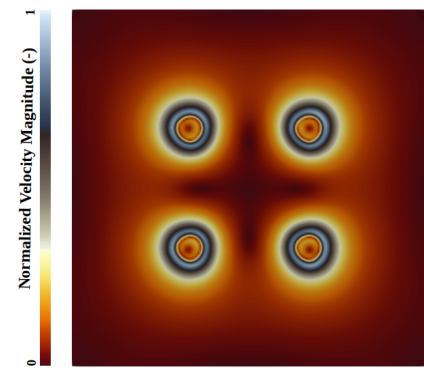
Figure 12 presents the case under reactive Stefan flow, excluding gas-phase mean flow, and focuses on the associated interfacial dynamics and mass transfer. The contour plots compare two different droplet configurations: two droplets (left column) and four droplets (right column), providing insights into the spatial distribution of key variables. The first row (Figures 12a,b) presents the normalized H₂O_(g) concentration in the gas phase, highlighting the evaporative distribution around the droplets. The concentration field reveals higher values at the droplet interface, where evaporation occurs, with diffusion-driven transport extending into the surrounding gas phase. The presence of multiple droplets alters the local concentration gradients, modifying the evaporation characteristics due to inter-droplet interactions. The second row (Figures 12c,d) displays the normalized velocity magnitude, illustrating the velocity field induced by reactive Stefan flow. The results reveal that reactive Stefan flow, driven by multiple droplets, induces intricate interactions that modify the system's velocity distribution and transport dynamics. These interactions give rise to distinct streamline patterns and localized convective motion near the droplets, with the overall flow behavior being contingent upon both the droplet number and their mutual interactions. The third row (Figures 12e,f) presents the normalized absorbed CO₂ concentration in the liquid phase, overlaid with velocity vectors to illustrate the interplay between reactive mass transfer and flow dynamics. The contours provide a detailed view of localized flow structures around the droplets and within the surrounding gas-phase environment. The results indicate that reactive Stefan flow has a comparatively weaker influence on CO₂ absorption than on



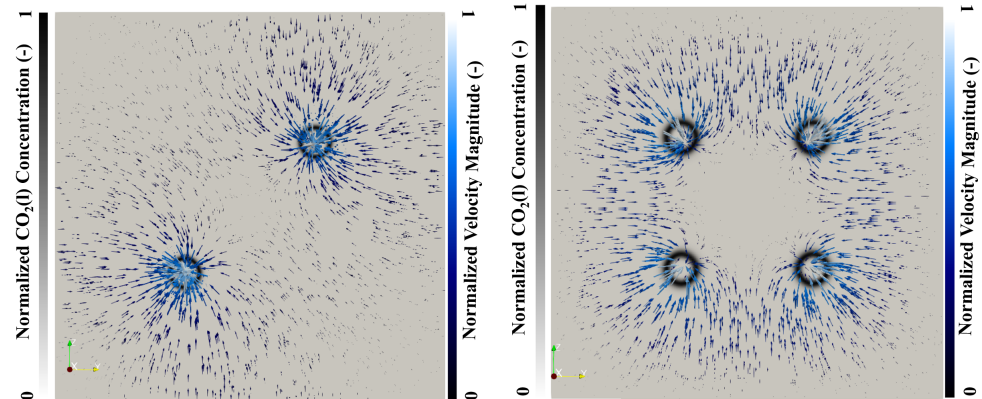
(a) Normalized $\text{H}_2\text{O}_{(g)}$ concentration in the gas phase (two droplets).



(c) Normalized velocity magnitude (two droplets).



(d) Normalized velocity magnitude (four droplets).



(e) Normalized absorbed CO_2 concentration in the liquid phase with velocity vectors (two droplets). (f) Normalized absorbed CO_2 concentration in the liquid phase with velocity vectors (four droplets).

Figure 12: Contour plots of key variables for two different droplet configurations: two droplets (left) and four droplets (right). (a, b) Normalized $\text{H}_2\text{O}_{(g)}$ concentration in the gas phase, showing the evaporative distribution. (c, d) Normalized velocity magnitude, highlighting flow variations induced by reactive Stefan flow and droplet interactions. (e, f) Normalized absorbed CO_2 concentration in the liquid phase overlaid with velocity vectors, demonstrating the impact of reactive Stefan flow on mass transfer dynamics, emphasizing localized flow structures after $t=10$ ms.

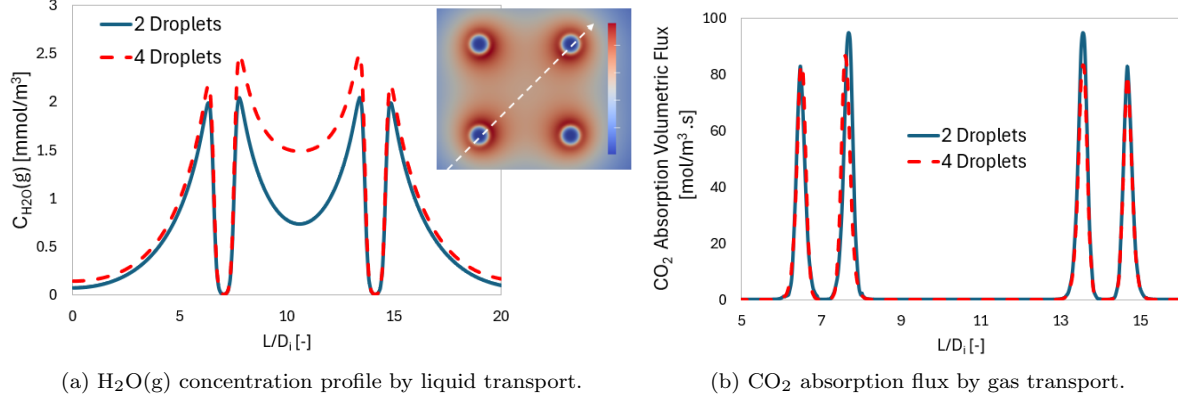


Figure 13: Effect of droplet number on H_2O vapor concentration and reactive CO_2 absorption flux under Stefan flow (no mean flow) conditions. Profiles are extracted along a diagonal transect intersecting two droplets in both two- and four-droplet systems. As droplet number increases, each droplet becomes increasingly influenced by both the surrounding ambient transport field and neighboring droplets, leading to modified vapor-phase coupling and asymmetry in interfacial absorption behavior.

water evaporation. This disparity arises due to the higher molar density of the liquid phase and the much lower diffusivity coefficient of CO_2 in the liquid, which limits mass transfer efficiency relative to water vapor transport. Differences between two- and four-droplet configurations reveal that inter-droplet interactions sensibly affect gaseous concentration fields and surrounding flow structures.

This comparison is further revealed through the interfacial flux profiles presented in Figure 13, which show the spatial variation of H_2O vapor concentration and CO_2 absorption flux along a diagonal transect intersecting two droplets in each configuration. In the vapor phase, the four-droplet case exhibits elevated background concentrations and asymmetrical peak distributions, indicating strong inter-droplet coupling resulting from overlapping diffusion fields. In contrast, the CO_2 absorption flux profiles remain sharply localized and nearly identical between the two- and four-droplet cases, suggesting that liquid-phase transport is less influenced by droplet proximity. A slight increase in absorption intensity in the four-droplet case may result from enhanced local cooling due to intensified evaporation, which reduces interface temperature and promotes gas solubility. This contrast highlights a fundamental transport asymmetry: evaporation is governed by long-range vapor-phase diffusion and inter-droplet interactions, whereas absorption is controlled by localized interfacial kinetics and constrained by the low diffusivity of CO_2 in the liquid phase.

4.6.2. Effect of Mean Flow on Reactive CO₂ Absorption

Compared to the no-mean-flow case, the addition of an imposed gas-phase velocity field, superimposed on the reactive Stefan flow, significantly alters the interfacial absorption dynamics. Figure 14 illustrates the effect of a mean flow with initial velocity $V_Y = 0.01$ m/s on the system, showing (a) pressure variation, (b) normalized CO₂(l) concentration, and (c) normalized MDEAH concentration in the liquid phase over two time intervals for the configuration with four droplets. All concentrations are normalized by their domain maxima for consistent comparison. As shown in Figure 14a, the imposed mean flow induces a

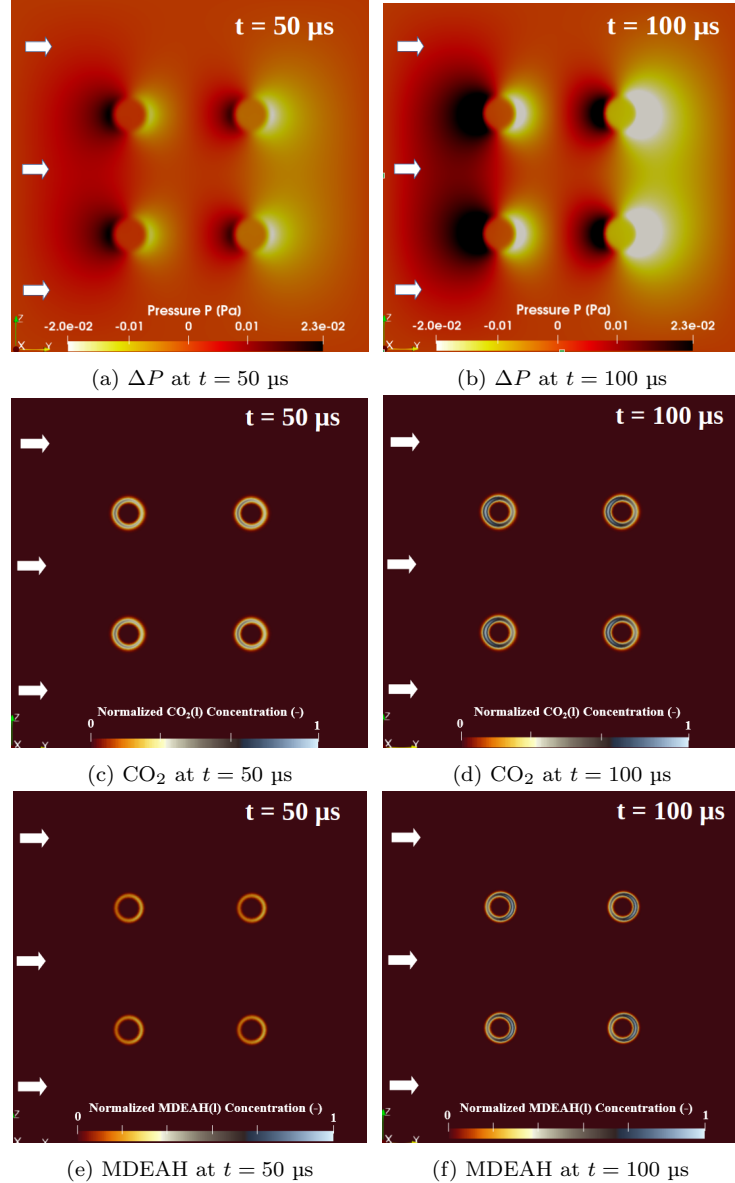


Figure 14: Contour maps of (a) pressure variation, (b) normalized CO₂(l) concentration, and (c) normalized MDEAH concentration in the liquid phase at an initial ambient velocity of $V_Y = 0.01$ m/s and $X_{\text{MDEA}} = 0.3$, across two time steps. Concentrations are normalized by their respective maximum values in the domain to facilitate comparison of interfacial distributions over time.

non-uniform pressure distribution around each droplet, characterized by elevated pressure on the upstream side and reduced pressure downstream, reflecting localized flow deflection and asymmetry in the surrounding field. These variations alter the interfacial transport conditions and influence species transfer in the liquid phase. In Figure 14b, the CO_2 concentration field becomes increasingly anisotropic, with enhanced convective transport altering concentration gradients near the interface. Although limited by the low liquid-phase diffusivity of CO_2 ($\sim 10^{-9} \text{ m}^2/\text{s}$), the absorption front grows steadily over time. Similarly, MDEAH distribution (Figure 14c) becomes increasingly shaped by convection, highlighting the role of flow in product redistribution and reaction-zone development. These changes demonstrate how even modest mean flows reshape the spatial and temporal characteristics of interfacial transport and reactive diffusion.

To further quantify these effects, Figure 15 presents CO_2 absorption flux profiles along a diagonal path intersecting two droplets under increasing mean flow velocities. As the imposed velocity increases from 0 to 5 mm/s, the intensification of absorption peaks indicates stronger convective transport near the interface, where the adjacent fluid is more effectively displaced and refreshed by the bulk flow, thereby enhancing mass transfer. The profiles also show increasing asymmetry, with higher flux observed on the downstream side of each droplet. This directional non-uniformity indicates that mean flow not only enhances overall absorption but also redistributes it unevenly across the droplet surface. These findings underscore the dual role of convection in amplifying interfacial fluxes and modifying their spatial structure—effects that become increasingly important in multi-droplet systems where localized interactions shape global mass transfer behavior.

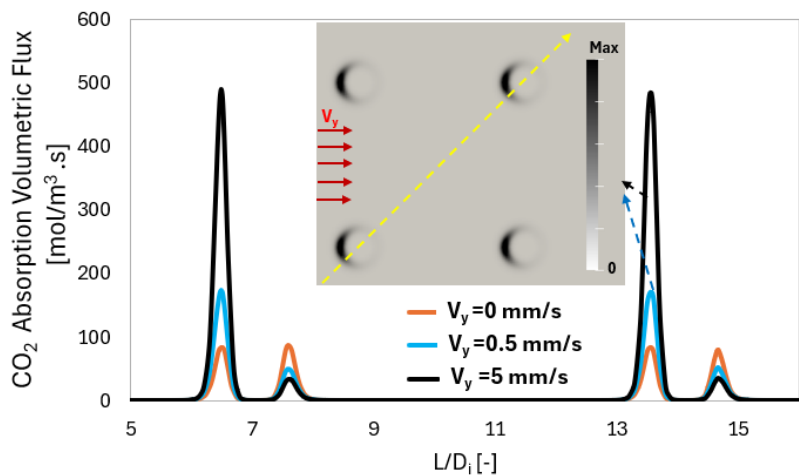


Figure 15: CO_2 volumetric absorption flux along a diagonal path intersecting two droplets, shown for different imposed mean flow velocities after 1 ms.

5. Conclusion

This study presents a comprehensive reactive two-phase mass and heat transfer model for simulating CO_2 absorption and desorption in the presence of water evaporation and condensation at the droplet scale. The model incorporates mass species transport equations for both phases through two scalar transport equations, along with a single equation for momentum and one-scalar equation for enthalpy, to simulate interfacial reactive dynamics in vapor-liquid equilibrium. The model balances the mass transfer between liquid and vapor, addressing non-ideal behavior in CO_2 capture by incorporating a variable apparent Henry constant. To track the liquid-gas interface, a conservative phase-field framework is employed, utilizing regularization techniques to minimize numerical diffusion at the interface. Additionally, it incorporates reactive Stefan flow to account for velocity discontinuities across the phase boundary, a feature often neglected in previous multiphase studies. Sensitivity analyses across multiple configurations reveal key mechanisms governing interfacial reactive mass transfer, highlighting a nonlinear coupling between convection, diffusion, phase change, and chemical reactions. The main findings are summarized as follows.

- **Single-droplet absorption:** Simulations reveal that interfacial transport and reaction processes compete across distinct time scales, shaping the multiscale absorption dynamics. Increasing MDEA mole fraction enhances reactivity but limits CO_2 diffusivity, resulting in a nonlinear absorption response.
- **Single-droplet desorption:** Desorption exhibits reversed transport-reaction dynamics, with higher MDEA loading reducing CO_2 release due to stronger binding. Notably, H_2O phase change (evaporation or condensation) has minimal effect on CO_2 uptake/release and contributes negligibly to the Stefan velocity, which remains governed by the interfacial reactive CO_2 transport.
- **Multi-droplet absorption without mean flow (pure reactive Stefan-driven regime):** Simulations of two- and four-droplet systems reveal that increasing the number of droplets—and thereby reducing inter-droplet spacing—intensifies vapor-phase coupling. Overlapping water vapor diffusion zones induce asymmetric evaporation fields, while CO_2 absorption remains localized due to low liquid-phase diffusivity and high molar density—demonstrating a phase asymmetry in inter-droplet coupling.
- **Multi-droplet absorption with imposed gas-phase mean flow:** In the presence of a uniform gas-phase mean flow, convection enhances gas-side mixing and steepens interfacial concentration gradients, increasing CO_2 absorption rates. The flow induces pressure and concentration asymmetries, shifting the absorption maxima to the downstream part of the droplets. In multi-droplet configurations, these convective effects interact with vapor-phase coupling, leading to spatially heterogeneous absorption patterns.

Numerically, the model exhibits strong flexibility and stability, as shown also in [24], enabling the resolution of the interfacial dynamics on relatively coarse grids within the DIM framework. While effective at capturing complex interface behavior, the approach

remains computationally intensive for systems with high diffusivity ratios (e.g., CO₂, where $D_g/D_l \sim 10^4$), emphasizing the need for more efficient solvers.

Although this study focuses on CO₂ absorption into aqueous MDEA, the framework is broadly applicable to other gas–liquid systems involving coupled interfacial mass, heat transfer, and chemical reactions. Future extensions will incorporate turbulence, dynamic surface tension, and turbulence–reaction coupling [47], enabling high-fidelity simulations of industrial-scale reactive two-phase flows.

Acknowledgments

The simulations and data management were carried out using resources provided by the National Academic Infrastructure for Supercomputing in Sweden (NAISS) at the PDC Center for High Performance Computing, with partial funding from the Swedish Research Council under grant agreement no. 2022-06725. Additional support was provided by the Swedish Research Council under grant agreement no. 2019-04086.

Appendix A. Desorption

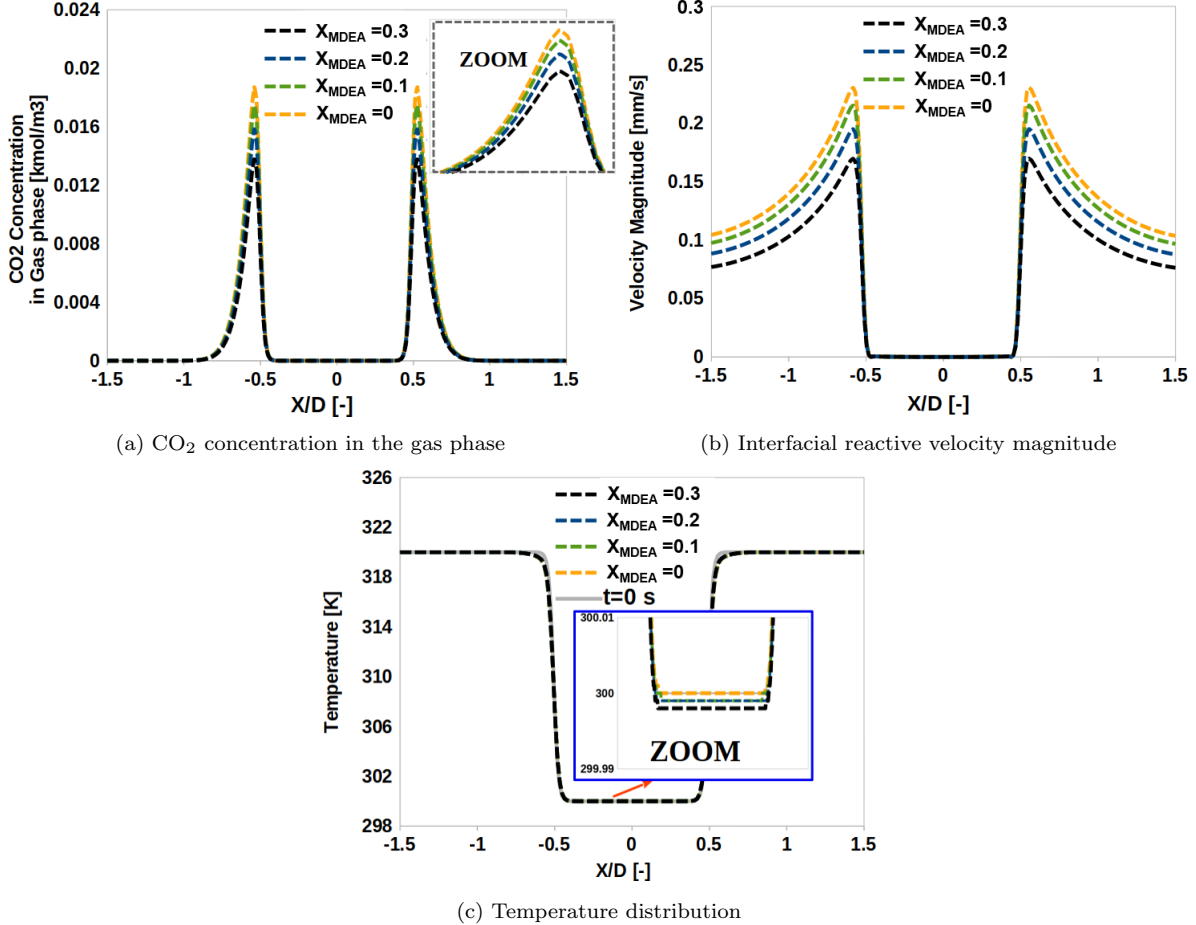


Figure A1: Spatial distribution of desorbed CO₂ concentration in the gas phase (a), Stefan (reactive) velocity magnitude (b), and temperature distribution (c) along the centerline axis of a single droplet with varying X_{MDEA} , after $t = 100 \mu\text{s}$.

Nonlinear behavior in the desorption process is primarily driven by variations in MDEA mole fraction. In the desorption scenario, as depicted in Fig. 1, CO₂ has dissolved in aqueous MDEA and is surrounded by gaseous steam, with the potential for both condensation and CO₂ desorption. Desorption initiates at the vapor–liquid interface, where a local peak in CO₂ concentration coincides with the maximum interfacial Stefan velocity, as illustrated in Figs. 4 and 5. Figures A1(a-c) illustrate the influence of MDEA mole fraction on CO₂ concentration in the gas phase, velocity, and temperature along the centerline. Increased MDEA mole fraction leads to reduced CO₂ desorption in the gas phase and mass transfer, driven by changes in diffusion coefficients and Henry’s law (Fig. A1(a)). This results in a decrease in velocity (Fig. A1(b)) and pressure fluctuation. Furthermore, as an endothermic process, CO₂ desorption absorbs heat, and higher MDEA mole fractions lead to greater temperature reduction (Fig. A1(c)), though this has little effect on steam condensation.

References

- [1] United Nations, Transforming our world: the 2030 agenda for sustainable development, A/RES/70/1, United Nations General Assembly, <https://sdgs.un.org/goals/goal7> (2015).
- [2] IPCC, Climate Change 2022: Impacts, Adaptation, and Vulnerability. Contribution of Working Group II to the Sixth Assessment Report of the Intergovernmental Panel on Climate Change, Cambridge University Press, Cambridge, UK and New York, NY, USA, 2022. [doi:10.1017/9781009325844](https://doi.org/10.1017/9781009325844).
- [3] J. Kuntz, A. Aroonwilas, Performance of spray column for co₂ capture application, *Industrial & Engineering Chemistry Research* 47 (1) (2008) 145–153. [doi:10.1021/ie0617021](https://doi.org/10.1021/ie0617021).
- [4] D. deMontigny, P. Tontiwachwuthikul, A. Chakma, Comparing the absorption performance of packed columns and membrane contactors, *Industrial & Engineering Chemistry Research* 44 (15) (2005) 5726–5732. [doi:10.1021/ie040264k](https://doi.org/10.1021/ie040264k).
- [5] A. Jamal, Absorption and desorption of CO₂ and CO in alkanolamine systems, Ph.D. thesis, University of British Columbia, Vancouver, BC, electronically available from <https://open.library.ubc.ca/media/download/pdf/831/1.0058971/2> (2002).
- [6] R. Ramezani, S. Mazinani, R. Di Felice, Density, viscosity, ph, heat of absorption, and co₂ loading capacity of methyldiethanolamine and potassium lysinate blend solutions, *J. Chem. Eng. Data* 66 (2021) 1611. [doi:10.1021/acs.jced.0c00855](https://doi.org/10.1021/acs.jced.0c00855).
- [7] X. M. Wu, Z. Qin, Y. S. Yu, Z. X. Zhang, Experimental and numerical study on co₂ absorption mass transfer enhancement for a diameter-varying spray tower, *Applied Energy* 225 (2018) 367–379. [doi:10.1016/j.apenergy.2018.04.053](https://doi.org/10.1016/j.apenergy.2018.04.053).
- [8] O. Cejpek, M. Maly, V. K. Dhinasekaran, M. M. Avulapati, L. Dacanay, J. Jedelsky, Novel atomizer concept for ccs applications: Impinging effervescent atomizer, *Separation and Purification Technology* 311 (2023) 123259. [doi:10.1016/j.seppur.2023.123259](https://doi.org/10.1016/j.seppur.2023.123259).
- [9] Y. Tamhankar, B. King, J. Whiteley, T. Cai, K. McCarley, M. Resetarits, C. Aichele, Spray absorption of co₂ into monoethanolamine: Mass transfer coefficients, dropsize, and planar surface area, *Chemical Engineering Research and Design* 104 (2015) 376–389. [doi:10.1016/j.cherd.2015.08.012](https://doi.org/10.1016/j.cherd.2015.08.012).
- [10] Y. Xu, X. Chen, Y. Zhao, B. Jin, Modeling and analysis of co₂ capture by aqueous ammonia + piperazine blended solution in a spray column, *Separation and Purification Technology* 267 (2021) 118655. [doi:10.1016/j.seppur.2021.118655](https://doi.org/10.1016/j.seppur.2021.118655).
- [11] J. Qu, N. Qi, K. Zhang, L. Li, P. Wang, Wet flue gas desulfurization performance of 330 mw coal-fired power unit based on computational fluid dynamics: Region identification of flow pattern and transfer process, *Chinese Journal of Chemical Engineering* 29 (2021) 13–26. [doi:10.1016/j.cjche.2020.08.004](https://doi.org/10.1016/j.cjche.2020.08.004).

- [12] L. Marocco, F. Inzoli, Multiphase euler–lagrange cfd simulation applied to wet flue gas desulphurisation technology, *International Journal of Multiphase Flow* 35 (2) (2009) 185–194. [doi:10.1016/j.ijmultiphaseflow.2008.09.005](https://doi.org/10.1016/j.ijmultiphaseflow.2008.09.005).
- [13] P. Tabarzadi, A. Ghaemi, Modeling and optimization of co₂ capture in spray columns via artificial neural networks and response surface methodology, *Case Studies in Chemical and Environmental Engineering* 10 (2024) 100783. [doi:https://doi.org/10.1016/j.cscee.2024.100783](https://doi.org/10.1016/j.cscee.2024.100783).
- [14] C. C. Chatziasteriou, E. S. Kikkinides, M. C. Georgiadis, Recent advances on the modeling and optimization of co₂ capture processes, *Computers & Chemical Engineering* 165 (2022) 107938. [doi:10.1016/j.compchemeng.2022.107938](https://doi.org/10.1016/j.compchemeng.2022.107938).
- [15] S. Mirjalili, C. B. Ivey, A. Mani, Comparison between the diffuse interface and volume of fluid methods for simulating two-phase flows, *International Journal of Multiphase Flow* 116 (2019) 221–238. [doi:10.1016/j.ijmultiphaseflow.2019.04.019](https://doi.org/10.1016/j.ijmultiphaseflow.2019.04.019).
- [16] S. Salimi Zamani, A. Mukherjee, M. Pelanti, L. Brandt, A low mach number diffuse-interface model for multicomponent two-phase flows with phase change, *Journal of Computational Physics* (2024). [doi:10.1016/j.jcp.2024.113683](https://doi.org/10.1016/j.jcp.2024.113683).
- [17] N. Scapin, F. Dalla Barba, G. Lupo, M. Rosti, C. Duwig, L. Brandt, Finite-size evaporating droplets in weakly compressible homogeneous shear turbulence, *J. Fluid Mech.* 934 (2022) A15. [doi:10.1017/jfm.2021.1140](https://doi.org/10.1017/jfm.2021.1140).
- [18] M. S. Baer, J. W. Nunziato, A two-phase mixture theory for the deflagration to detonation (ddt) transition in reactive granular materials, *International Journal of Multiphase Flow* 12 (6) (1986) 861–889. [doi:10.1016/0301-9322\(86\)90033-9](https://doi.org/10.1016/0301-9322(86)90033-9).
- [19] R. Saurel, C. Pantano, Diffuse-interface capturing methods for compressible two-phase flows, *Annual Review of Fluid Mechanics* (2018) 105–130 [doi:10.1146/annurev-fluid-122316-050109](https://doi.org/10.1146/annurev-fluid-122316-050109).
- [20] S. Yang, Modeling of diesel injection in subcritical and supercritical conditions, Ph.d. thesis, Université Paris Saclay (ComUE), fluids Mechanics [physics.class-ph], English. Available at: TEL Archives, NNT: 2019SACL045ff, <https://tel.archives-ouvertes.fr/tel-02296577> (2019).
- [21] P. Yi, S. Yang, C. Habchi, R. Lugo, A multicomponent real-fluid fully compressible four-equation model for two-phase flow with phase change, *Physics of Fluids* 31 (2) (2019) 026102. [doi:10.1063/1.5065781](https://doi.org/10.1063/1.5065781).
- [22] S. Jafari, H. Gaballa, C. Habchi, J. de Hemptinne, Exploring the interaction between phase separation and turbulent fluid dynamics in multi-species supercritical flow jets using a tabulated real-fluid model, *The Journal of Supercritical Fluids* (2022) 105557 [doi:10.1016/j.supflu.2022.105557](https://doi.org/10.1016/j.supflu.2022.105557).

- [23] H. Gaballa, S. Jafari, C. Habchi, J. C. de Hemptinne, Numerical investigation of droplet evaporation in high-pressure dual-fuel conditions using a tabulated real-fluid model, *International Journal of Heat and Mass Transfer* (2022). [doi:10.1016/j.ijheatmasstransfer.2022.122671](https://doi.org/10.1016/j.ijheatmasstransfer.2022.122671).
- [24] S. Mirjalili, S. S. Jain, A. Mani, A computational model for interfacial heat and mass transfer in two-phase flows using a phase-field method, *Int. J. Heat Mass Transf.* 197 (2022) 123326. [doi:10.1016/j.ijheatmasstransfer.2022.123326](https://doi.org/10.1016/j.ijheatmasstransfer.2022.123326).
- [25] M. S. Dodd, D. Mohaddes, A. Ferrante, M. Ihme, Analysis of droplet evaporation in isotropic turbulence through droplet-resolved dns, *International Journal of Heat and Mass Transfer* 172 (2021) 121157. [doi:10.1016/j.ijheatmasstransfer.2021.121157](https://doi.org/10.1016/j.ijheatmasstransfer.2021.121157).
- [26] H. A. Al-Ghawas, D. P. Hagewiesche, G. Ruiz-Ibanez, O. C. Sandall, Physicochemical properties important for carbon dioxide absorption in aqueous methyldiethanolamine, *Journal of Chemical Engineering Data* 34 (1989) 385–391. [doi:10.1021/je00058a004](https://doi.org/10.1021/je00058a004).
- [27] H. Kierzkowska-Pawlak, A. Chacuk, Kinetics of CO_2 desorption from aqueous n-methyldiethanolamine solutions, *Chemical Engineering Journal* 168 (2011) 367–375. [doi:10.1016/j.cej.2011.01.039](https://doi.org/10.1016/j.cej.2011.01.039).
- [28] S. S. Jain, Accurate conservative phase-field method for simulation of two-phase flow, *Journal of Computational Physics* 469 (2022) 111529. [doi:10.1016/j.jcp.2022.111529](https://doi.org/10.1016/j.jcp.2022.111529).
- [29] P. Vanýsek, Ionic Conductivity and Diffusion at Infinite Dilution, 1992nd Edition, CRC Press, Boca Raton, 1992.
- [30] P. Linstrom, W. Mallard, The NIST chemistry webbook: A chemical data resource on the internet, *Journal of Chemical and Engineering Data* 46 (5) (2001) 1059–1063.
- [31] J. Monteith, M. Unsworth, Principles of Environmental Physics, 3rd Edition, AP, Amsterdam, 2008.
- [32] T. L. Donaldson, Y. N. Nguyen, Carbon dioxide reaction kinetics and transport in aqueous amine membranes, *Industrial & Engineering Chemistry Fundamentals* 19 (1980) 260–266. [doi:10.1021/i160075a005](https://doi.org/10.1021/i160075a005).
- [33] A. Jamal, A. Meisen, C. Jim Lim, Kinetics of carbon dioxide absorption and desorption in aqueous alkanolamine solutions using a novel hemispherical contactor-ii: Experimental results and parameter estimation, *Chemical Engineering Science* 61 (2006) 6590–6603. [doi:10.1016/j.ces.2006.04.047](https://doi.org/10.1016/j.ces.2006.04.047).
- [34] M. J. Mitchell, O. E. Jensen, K. A. Cliffe, M. M. Maroto-Valer, A model of carbon dioxide dissolution and mineral carbonation kinetics, *Proceedings: Mathematical, Physical and Engineering Sciences* 466 (2117) (2010) 1265–1290. [doi:10.1098/rspa.2009.0349](https://doi.org/10.1098/rspa.2009.0349).

- [35] COMSOL, Chemical Reaction Engineering Module User's Guide, COMSOL, Inc., version 2018 (2018).
- [36] H. Liu, C. Yao, Y. Zhao, G. Chen, Desorption of carbon dioxide from aqueous mdea solution in a microchannel reactor, *Chemical Engineering Journal* (2016). [doi:10.1016/j.cej.2016.09.010](https://doi.org/10.1016/j.cej.2016.09.010).
- [37] Y. Zheng, E. El Ahmar, M. Simond, K. Ballerat-Busserolles, P. Zhang, CO₂ heat of absorption in aqueous solutions of mdea and mdea/piperazine, *Journal of Chemical & Engineering Data* 65 (8) (2020) 3784–3793. [doi:10.1021/acs.jced.9b01163](https://doi.org/10.1021/acs.jced.9b01163).
- [38] N. Scapin, P. Costa, L. Brandt, A volume-of-fluid method for interface-resolved simulations of phase-changing two-fluid flows, *Journal of Computational Physics* 407 (2020) 109251. [doi:10.1016/j.jcp.2020.109251](https://doi.org/10.1016/j.jcp.2020.109251).
- [39] M. Dodd, Direct numerical simulation of droplet-laden isotropic turbulence, Ph.D. thesis, University of Washington (2017).
- [40] T. Bergman, A. Lavine, F. Incropera, D. Dewitt, *Fundamentals of Heat and Mass Transfer*, Wiley, 2016, instructor 201609.
- [41] F. Ozkan, A. Wenka, E. Hansjosten, P. Pfeifer, B. Kraushaar-Czarnetzki, Numerical investigation of interfacial mass transfer in two-phase flows using the vof method, *Engineering Applications of Computational Fluid Mechanics* 10 (1) (2016) 100–110. [doi:10.1080/19942060.2015.1061555](https://doi.org/10.1080/19942060.2015.1061555).
- [42] M. S. Dodd, A. Ferrante, A fast pressure-correction method for incompressible two-fluid flows, *Journal of Computational Physics* 273 (2014) 416–434. [doi:10.1016/j.jcp.2014.05.024](https://doi.org/10.1016/j.jcp.2014.05.024).
- [43] S. Z. Salimi, A. Mukherjee, M. Pelanti, L. Brandt, A low mach number diffuse-interface model for multicomponent two-phase flows with phase change, *Journal of Computational Physics* 523 (2025) 113683. [doi:10.1016/j.jcp.2024.113683](https://doi.org/10.1016/j.jcp.2024.113683).
- [44] W.-H. Chen, M.-H. Tsai, C.-I. Hung, Numerical prediction of CO₂ capture process by a single droplet in alkaline spray, *Applied Energy* 109 (2013) 125–134. [doi:10.1016/j.apenergy.2013.03.082](https://doi.org/10.1016/j.apenergy.2013.03.082).
- [45] M. Ouboukhlik, G. Godard, S. Saengkaew, M.-C. Fournier-Salaün, L. Estel, G. Grehan, Mass transfer evolution in a reactive spray during carbon dioxide capture, *Chemical Engineering & Technology* 38 (2015) 1154–1164. [doi:10.1002/ceat.201400651](https://doi.org/10.1002/ceat.201400651).
- [46] G. Han, [Experimental and numerical study of co₂ absorption into single droplets and liquid films](#), Ph.D. thesis, University College of Southeast Norway (2014).
URL <https://openarchive.usn.no/usn-xmlui/handle/11250/2437779>
- [47] A. Najarnezhad mashhadi, S. Jafari, C. Häggmark, H. Kusar, C. Duwig, Co₂ absorption in industrial multi-nozzle spray towers: Cfd and experimental study of flow and mass transfer dynamics, manuscript submitted for publication (2025).